Journal of Power Sources 653 (2025) 237539

Contents lists available at ScienceDirect

Journal of Power Sources

journal homepage: www.elsevier.com/locate/jpowsour

# Modeling chemo-thermal mechanical stresses in all-solid-state lithium Batteries: Influence of grain morphology and alignment

Fadi Al-Jaljouli [a,b,*], Robert Mücke [a], Martin Finsterbusch [a,e], Payam Kaghazchi [a,d], Olivier Guillon [a,b,c,e]

[a] Forschungszentrum Jülich GmbH, Institute of Energy Materials and Devices, Materials Synthesis and Processing (IMD-2), 52425, Jülich, Germany
[b] Institute of Mineral Engineering, RWTH Aachen University, 52064, Aachen, Germany
[c] Jülich Aachen Research Alliance: JARA-Energy, Jülich, 52425, Germany
[d] MESA+ Institute for Nanotechnology, University of Twente, P. O. Box 217, Enschede, 7500AE, the Netherlands
[e] Helmholtz Institute Münster: Ionics in Energy Storage (IMD-4 / HI MS), Münster, 48149, Germany

## HIGHLIGHTS

- Randomly aligned fiber LLZO with hexagonal LCO slightly reduces induced stresses.
- Contact with specific hexagonal LCO facets strongly affects stress distribution.
- The alignment of LLZO fibers plays a critical role in determining the stress state.
- Anisotropic expansion–contraction behavior of LCO contributes to stress mitigation.
- Randomly oriented spherical LCO leads to the highest mechanical stress.

## ARTICLE INFO

*Keywords:*
All-solid-state lithium batteries
Grain morphology
Garnet electrolyte
Cathode active material
Microstructural design parameters

## ABSTRACT

All-solid-state batteries (ASSBs) are gaining attraction as a safer and more efficient alternative to traditional liquid lithium-ion batteries due to their use of solid electrolytes. However, the advancement of ASSBs is hindered by challenges such as mechanical stress induced by volume changes in the cathode active material (CAM) during cycling. This study investigates the impact of composite cathode grain morphology on the induced mechanical stress within the composite cathode, specifically focusing on the configurations involving spherical and hexagonal $LiCoO_2$ (LCO) paired with spherical and fiber-shaped garnet-type $Li_7La_3Zr_2O_{12}$ (LLZO) electrolytes. Four distinct systems are analyzed: spherical LCO-spherical LLZO, spherical LCO-fiber LLZO, hexagonal LCO-spherical LLZO, and hexagonal LCO-fiber LLZO. By generating modeled microstructures, we investigate the effects of the solid volume fraction of LCO and porosity on the induced chemo-thermal mechanical stress, reflecting real-life scenarios considering induced stresses after sintering. Our findings reveal that fiber LLZO in conjunction with textured hexagonal LCO reduces the induced mechanical stress in both components by 11.0 % for LCO and 9.0 % for LLZO. In contrast, the use of randomly oriented spherical LCO in the composite leads to higher induced mechanical stresses in both LCO and LLZO. The alignment of fiber LLZO critically influences the stress type within the system due to facet-specific contact interfaces, underscoring the importance of grain morphology in optimizing the mechanical performance of ASSBs.

## 1. Introduction

All-solid-state batteries (ASSBs) have attracted considerable research attention as a promising alternative to conventional liquid lithium-ion batteries (LIBs). Due to the use of solid electrolytes replacing liquid electrolytes, ASSBs offer enhanced safety and higher energy density

* Corresponding author. Forschungszentrum Jülich GmbH, Institute of Energy Materials and Devices, Materials Synthesis and Processing (IMD-2), 52425, Jülich, Germany
*E-mail addresses:* f.al-jaljouli@fz-juelich.de (F. Al-Jaljouli), r.muecke@fz-juelich.de (R. Mücke), m.finsterbusch@fz-juelich.de (M. Finsterbusch), p.kaghazchi@fz-juelich.de (P. Kaghazchi), o.guillon@fz-juelich.de (O. Guillon).

https://doi.org/10.1016/j.jpowsour.2025.237539
Received 21 March 2025; Received in revised form 17 May 2025; Accepted 1 June 2025
Available online 3 July 2025

[1–3] by enabling the coupling of high-capacity electrode materials like Li metal, they contribute to higher energy densities. However, the advancement of ASSBs is still impeded by critical challenges, including the formation of detrimental chemical reactions at the interface between the cathode active material and the solid electrolyte [4–6]. Moreover, the formation of dendrites under high current continues to pose a significant and persistent challenge for researchers. [7–10]. The significant degradation observed during cycling, attributed to mechanical fatigue [11–13], also remains an unresolved challenge.

The cathode plays a critical role in determining the areal capacity and energy density in ASSBs. To achieve high energy ASSBs, a thick composite cathode is utilized, consisting of intertwined solid electrolyte and cathode active material (CAM) particles. This configuration ensures percolating pathways for efficient ion and electron transport. However, the application of stiff solid electrolytes introduces a significant drawback, as their rigidity constrains the volume changes of the active material during cycling, which is the primary cause of mechanical stress within the composite cathode, potentially inducing microcracks propagating throughout the entire cell [14–16], which in turn leads to capacity fade.

Researchers have applied various strategies to mitigate induced mechanical stresses, emphasizing the development of CAMs. The introduction of so-called "zero-strain" CAMs (NCM271 and NCM361) is one such approach. However, these materials do not keep a constant volume and are anisotropic during the delithiation process. [17–19]. While the mixing of CAMs with opposite strain signs (e.g., LCO with NCM) achieves a net zero strain at the component level, it continues to induce stresses at the grain level. [20]. The scope of efforts has broadened to include the incorporation of additives as an additional approach. Researchers have found that integrating elastomer binders into the composite cathode can reduce induced mechanical stresses, but this reduction is accompanied by a decrease in capacity, which limits the use of elastomer binders to low concentrations [21,22]. He, YaoLong et al. reported a capacity fade of the graphite and silicon anodes ascribed to stresses within the solid electrolyte interphase [23].

$LiCoO_2$ (LCO) is particularly noted for its remarkable stability and high capacity among CAMs composed of layered transition metal oxides [24–28]. It exhibits a hexagonal layered α-$NaFeO_2$ structure where the layers of octahedra $CoO_6$ are aligned perpendicular to the c-axis, corresponding to the {001} facets. In contrast, the hexagonal crystal's six-sided facets, indexed as {010} facets, are oriented perpendicular to the {001} planes (Fig. 1). Nevertheless, LCO is associated with several negative aspects, including toxicity and high materials costs. Furthermore, its inherent structural instability detrimentally impacts its electrochemical performance, resulting in a practical capacity that is only approximately 50 % of its theoretical potential [29,30].

Garnet-type $Li_7La_3Zr_2O_{12}$ (LLZO) with different dopants such as Al and Ta has garnered considerable attention from researchers within the broad spectrum of solid lithium-ion conductors. This material is distinguished by its high ionic conductivity, which can exceed 1 mS/cm at room temperature, and its inherently low electronic conductivity. Furthermore, LLZO possesses a broad electrochemical stability window and exhibits exceptional chemical and electrochemical stability when interfaced with lithium metal [31–35].

The thermodynamic stability of LLZO/CAM mixtures is driven by the necessity of high-temperature co-sintering of the solid electrolyte (SE) and cathode active material (CAM) at temperatures above 1000 °C. This high-temperature requirement poses significant challenges, primarily due to material compatibility issues and formation of interdiffusion layers as a result of undesirable side reactions among interface between LLZO and LCO which might lead to degradation of the cell's electrochemical performance ascribed to hindering of the de-/lithiation process. Which have been widely studied by various research groups [36–38].

Among the various CAMs used in LIBs, LCO has demonstrated thermodynamic stability when combined with LLZO at elevated temperatures. In contrast, other CAMs such as NCM, $LiNi_{0.8}Co_{0.15}Al_{0.05}O_2$ (NCA), $LiMn_2O_4$ (LMO) and $LiFePO_4$ (LFP) react with LLZO at moderate temperatures between 400 °C and 800 °C.

Grain morphologies have been the focus of limited research. Jeon et al. concluded that the shape and facet design of CAMs significantly influence solid-solid ion migration, suggesting that single-crystalline octahedral NCM particles enhance Li-ion diffusion at the interface between the solid electrode and solid electrolyte in ASSBs [39]. Meanwhile, Wu et al. found that LCO flakes exhibit high specific capacity, excellent rate performance, and remarkable cycling stability over a wide range of operating temperatures [40].

Despite various studies investigating the effect of fiber LLZO in the solid electrolyte [41–45], none of the previous researches has addressed the impact of component grain morphologies on the induced mechanical stress in ASSBs.

In this research, we investigate the effect of composite cathode grain morphology on the induced mechanical stress within the composite cathode. Model microstructures were generated, incorporating spherical

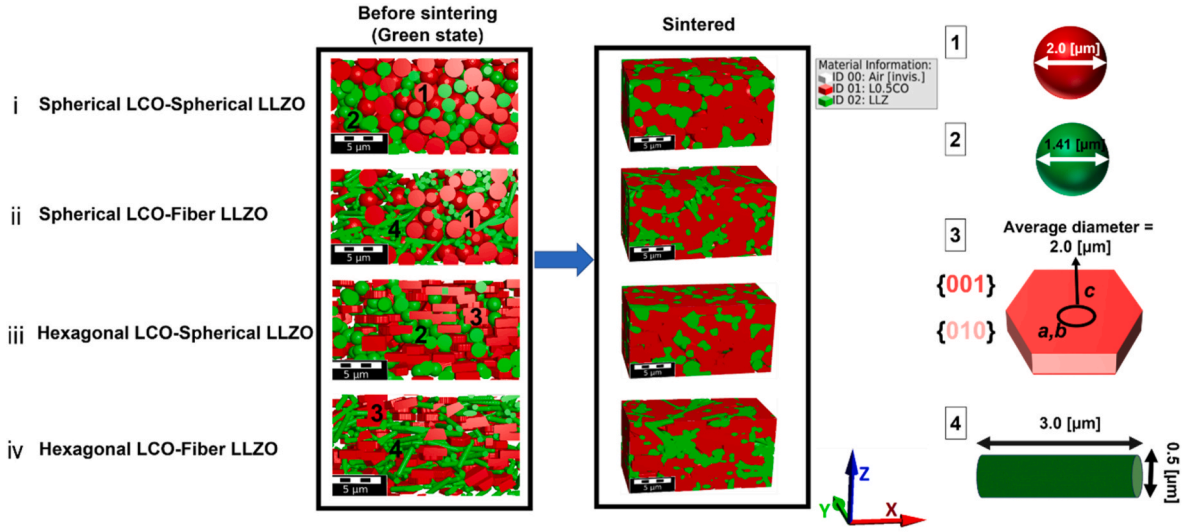


**Fig. 1.** Generated modeled microstructure utilizing different LCO and LLZO morphologies: (i) spherical LCO–spherical LLZO, (ii) spherical LCO–fiber LLZO, (iii) hexagonal LCO-spherical LLZO, and (iv) hexagonal LCO-fiber LLZO. The assigned lattice facets of hexagonal LCO are indicated. The initial average grain sizes of LCO and LLZO 2.00 μm and 1.41 μm, respectively. Fiber LLZO length and diameters 3 μm and 0.5 μm respectively, $SVF_{LCO} = 69.4$ % and $\bar{\rho} = 93.14$ %.

and hexagonal shapes of LCO alongside spherical and fiber-shaped LLZO. This approach leads to the formation of four distinct systems: spherical LCO-spherical LLZO, spherical LCO-fiber LLZO, hexagonal LCO-spherical LLZO, and hexagonal LCO-fiber LLZO. For each configuration, we analyze the effects of the solid volume fraction of LCO and the porosity on the induced chemo-thermal mechanical stress, which accurately reflects real-life scenarios, as it considers the mechanical stress induced by cooling down to room temperature after sintering. Additionally, we examine the impact of the random orientation of spherical LCO and the alignment of fiber LLZO on the type and magnitude of the induced mechanical stress. Notably, this research excludes the effects of grain sizes for both the CAM and SE, since our previous study demonstrated that the induced mechanical stress is independent from the grain size of the microstructural components [46].

## 2. Methods

### 2.1. Synthesis and acquisition of experimental structure

The composite cathode, consisting of $LiCoO_2$ (LCO) and Ta, Al-doped LLZO (abbreviated as LLZO, $Li_{6.45}Al_{0.05}La_3Zr_{1.6}Ta_{0.4}O_{12}$) in a mass ratio of 2:1, was synthesized through a modified solid-state reaction (SSR) method, as described previously [47,48]. Subsequently, focused ion beam (FIB) SEM stack images of the cross section were acquired, yielding an isotropic voxel size of 50 nm. These images were then subjected to a sequence of computational methods to generate a model of the experimental structure. The processing details are thoroughly explained in Ref. [49].

### 2.2. Characteristics of the microstructure

Solid volume fraction of LCO ($SVF_{LCO}$) can be defined as the ratio of LCO to the relative density $\overline{\rho}$ ,which is defined as the sum of volume ratio of LCO ($\overline{V}_{LCO}$) with the volume fraction of LLZO ($\overline{V}_{LLZO}$) in the composite cathode.

$$SVF_{LCO} = \frac{\overline{V}_{LCO}}{\overline{\rho}} \tag{1}$$

$$\overline{\rho} = \overline{V}_{LCO} + \overline{V}_{LLZO} \tag{2}$$

$$\overline{V}_{LCO} = \frac{n v_{LCO}}{V_{Total}} \tag{3}$$

$$\overline{V}_{LLZO} = \frac{m v_{LLZO}}{V_{Total}} \tag{4}$$

Where $n$ and $m$ are the number of LCO and LLZO grains respectively, while $v_{LCO}$ and $v_{LLZO}$ are the volume of each grain of LCO and LLZO respectively.

### 2.3. Generation of model microstructure

The composite cathode microstructure was generated using GeoDict software, utilizing a Python script, as described in Ref. [46]. Initially, populating a domain of 400 × 200 × 300 voxels (voxel length = 50 nm) with LCO and LLZO grains. The initial solid volume fraction of LCO was set at 69.4 %. In the generated systems utilizing hexagonal-shaped LCO, the hexagonal grains were horizontally aligned (parallel to the XY-plane) (Fig. 1) within the modeled sample to align with experimental observations [49]. The average grain diameters and fiber dimensions are listed in Fig. 1. Thereafter, a distribution step was implemented to ensure a homogeneous distribution of the microstructural components within the system. In order to ensure the representativeness of the generated structure, regions exhibiting inhomogeneity in either solid components or pores were eliminated. Followed by sintering process utilizing the Voronoi tessellation algorithm in GeoDict [50] to achieve the targeted density value of 93.14 %. The initial values of the solid volume fraction of LCO and relative density may be readjusted to ensure that the resulting values for both parameters exhibit a maximum deviation of 0.25 % from the target values. Fig. 1 shows the generated structures.

### 2.4. Materials parameters

To capture realistic behavior, our mechanical calculations were based on the induced chemo-thermal strains. These strains result from the superposition of thermal strains, generated after sintering due to the mismatch in the thermal expansion coefficients between LCO and LLZO [51] and electrochemically-induced strains. Furthermore, the calculations considered the input parameters of $Li_xCO$ with half lithium concentration (x = 0.5).

Theoretical DFT calculations by Yamakawa et al. [52] of the stiffness matrix of half delithiated LCO were adopted for our calculations due to the absence of experimental data. The stiffness matrix of $Li_{0.5}CoO_2$, as well as the Young's modulus and Poisson's ratios for LLZO, are summarized in Table 1.

From chemo-thermal strain calculations, the layered structure of LCO exhibits an expansion along c-axis, while contracting in both a and b-axes. Meanwhile, LLZO undergoes uniform contraction in all directions. The chemo-thermal strain values for $Li_{0.5}CO$ and LLZO are listed in Table 2.

The average principal stress $\overline{\boldsymbol{S}}_{\mathbf{all}}$ and the standard deviation $\boldsymbol{\Delta S}$, which represents the distribution's width, were calculated through a MATLAB script specifically developed to process output data from the ElastoDict FeelMath-LD module within GeoDict, developed by Math2-Market GmbH. [56,57]. Symmetric (Dirichlet) boundary conditions were imposed in all directions. The calculations assumed small deformation, as all observed deformations are less than 5 %. Furthermore, we assumed a homogenous charging (low C-rate), which in turn leads to a homogenous stress distribution across the microstructure. The geometric microstructures are found to be representative with a margin of error 2 % for LCO and 5 % for LLZO (Fig. S1).

### 2.5. Varying microstructural design parameters

To investigate the effect of grain morphology on the induced mechanical stress in the composite cathode, it is crucial to analyze how each modeled structure with different grain morphologies behaves while varying the environment of the structure specifically in this case, the solid volume fraction of LCO and the relative density. A similar approach was employed in Ref. [46], where one parameter of interest was varied while fixing the other, followed by mechanical characterization for each variation set. This method clearly reveals the effect of the investigated parameter by isolating the impact of the fixed parameters. The reference for our comparison in this research is the hexagonal LCO-spherical LLZO configuration, as it represents the experimentally achieved microstructure. The solid volume fraction of LCO lies between 20 and 95 % (Fig. 2), while relative density is within 40–95 % (Fig. 3). Worth mentioning is that the practical range of solid volume fraction for CAM in experimental cells generally falls between 33 % and 66 %. While through optimized and pressure-assisted sintering, relative density values are typically achieved within the range of 80 %–95 %. In case of unoptimized free sintering, the relative density values typically range from 45 % to 70 %. this comparison shows how simulation can enlarge the range of investigated parameters.

### 2.6. Mathematical formula of induced mechanical stress

The main contributor to induced mechanical stress in composite cathodes of ASSBs is the volume change which occurs during the cooling phase after sintering for both LCO and LLZO, as well as during the de-/

**Table 1**
Anisotropic stiffness matrix C, Young's modulus E, and Poisson ratio $\nu$ for $L_{0.5}CoO_2$ and LLZO.

| Material | Elastic parameter | Ref |
|---|---|---|
| **$Li_{0.5}CoO_2$** | $C = \begin{bmatrix} 303.86 & 101.71 & 32.58 & 0 & 7.31 & 0 \\ & 318.93 & 28.66 & 0 & -3.93 & 0 \\ & & 98.93 & 0 & 7.03 & 0 \\ & sym. & & 18.02 & 0 & -2.46 \\ & & & & 15.73 & 0 \\ & & & & & 101.94 \end{bmatrix}$ GPa | [52] |
| **LLZO** | E = 146 GPa, $\nu = 0.26$ | [53–55] |

**Table 2**
Crystallographic chemo-thermal strains for $L_{0.5}CoO_2$ in a-and c-axes and for LLZO.

| Material | $\epsilon^{chemo-thermal}$ | Ref |
|---|---|---|
| **$Li_{0.5}CoO_2$** | $\epsilon^a = -1.76 \times 10^{-2}$<br>$\epsilon^c = 2.38 \times 10^{-4}$ | [46] |
| **LLZO** | $-1.42 \times 10^{-2}$ | [46] |

lithiation phase for LCO. In both instances, the volume change in LCO is constrained by the neighboring LLZO, leaving the components of the microstructure to suffer from induced mechanical stress. Consequently, strain values are critical in determining the volume changes of the composite cathode components.

The total strain of LCO ($\epsilon_{LCO}$) in given direction (a, b and c-axes) can be expressed as:

$$(\epsilon_{LCO})_i = (\epsilon^{Li}_{LCO})_i + (\epsilon^{Th}_{LCO})_i + (\epsilon^{El}_{LCO})_i \ (i = a, b, c) \quad (5)$$

Where, $\epsilon^{Li}_{LCO}$, $\epsilon^{Th}_{LCO}$ and $\epsilon^{El}_{LCO}$ are the lithiation, thermal and elastic strains of LCO.

In contrast, no volume change is observed in LLZO during cycling. Thus, the total strain of LLZO ($\epsilon_{LLZO}$) in given direction (a, b and c-axes) can be expressed as:

$$(\epsilon_{LLZO})_i = (\epsilon^{Th}_{LLZO})_i + (\epsilon^{El}_{LLZO})_i \quad (6)$$

Where $\epsilon^{Th}_{LLZO}$ and $\epsilon^{El}_{LLZO}$ are the thermal and elastic strains of LLZO phases, respectively.

The elastic strains of LCO and LLZO are related to the stresses according to Hooke's law:

$$\sigma^i_{LCO} = \sum_j C^{ij} (\epsilon^{El}_{LCO})_j \quad (7)$$

$$\sigma^i_{LLZO} = E(\epsilon^{El}_{LLZO})_i \quad (8)$$

In this research, we did not consider any interface zones between CAM/SE due to lack of intrinsic mechanical parameters of formed interface zone.

## 3. Result and discussion

### 3.1. Effect of grain morphology with varying solid volume fraction of LCO

#### 3.1.1. Spherical vs. hexagonal LCO-spherical LLZO

Increasing the solid volume fraction of LCO reduces the presence of LLZO grains in the microstructure, which are then replaced by LCO grains. The primary advantage of increasing the LCO solid volume fraction is the reduction of mechanical stress in the LCO, as fewer constraints from the LLZO grains allow the LCO to undergo volume changes more freely. On the other hand, the remained LLZO grain content suffers from an induced tensile mechanical stress [46]. However, when spherical LCO particles are randomly oriented, the induced mechanical stress of LCO is entirely reversed, that is, it increases in parallel with the rise in

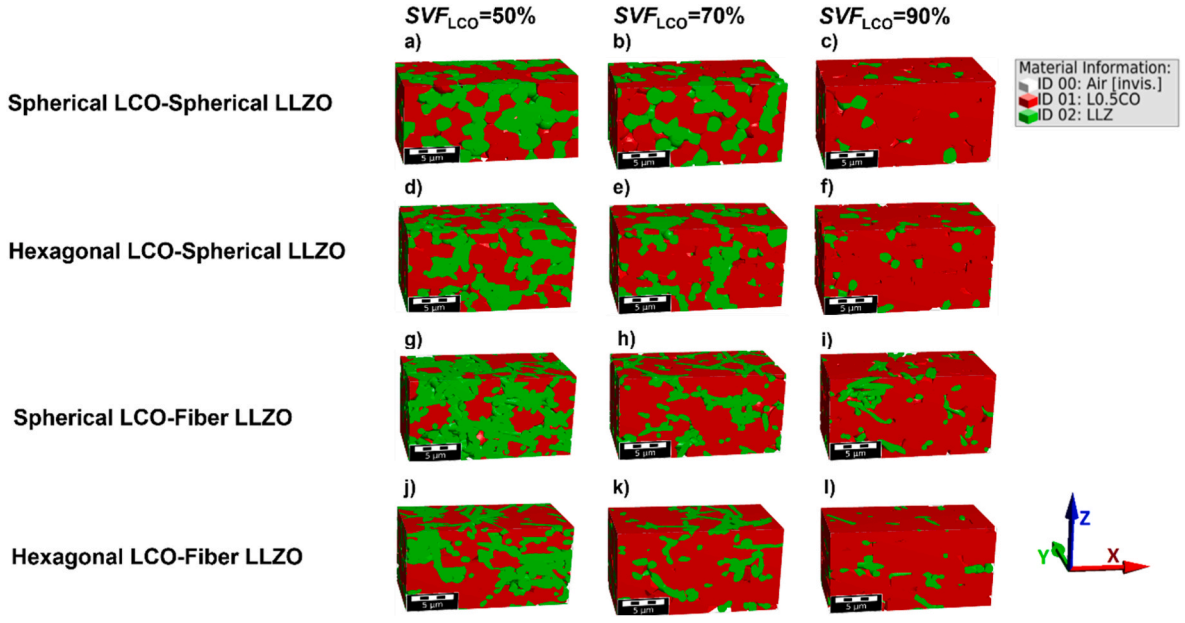


**Fig. 2.** Variation of $SVF_{LCO}$ only (50, 70 and 90 %), a-c) spherical LCO-spherical LLZO d-f) hexagonal LCO-spherical LLZO g-i) spherical LCO-fiber LZO j-l) hexagonal LCO-fiber LLZO. The fixed parameter values were as follow: $\bar{\rho} = 93.14\%$, average grain size of LCO and LLZO 2.00 μm and 1.43 μm, respectively, fiber LLZO length and diameters 3 μm and 0.5 μm, respectively.

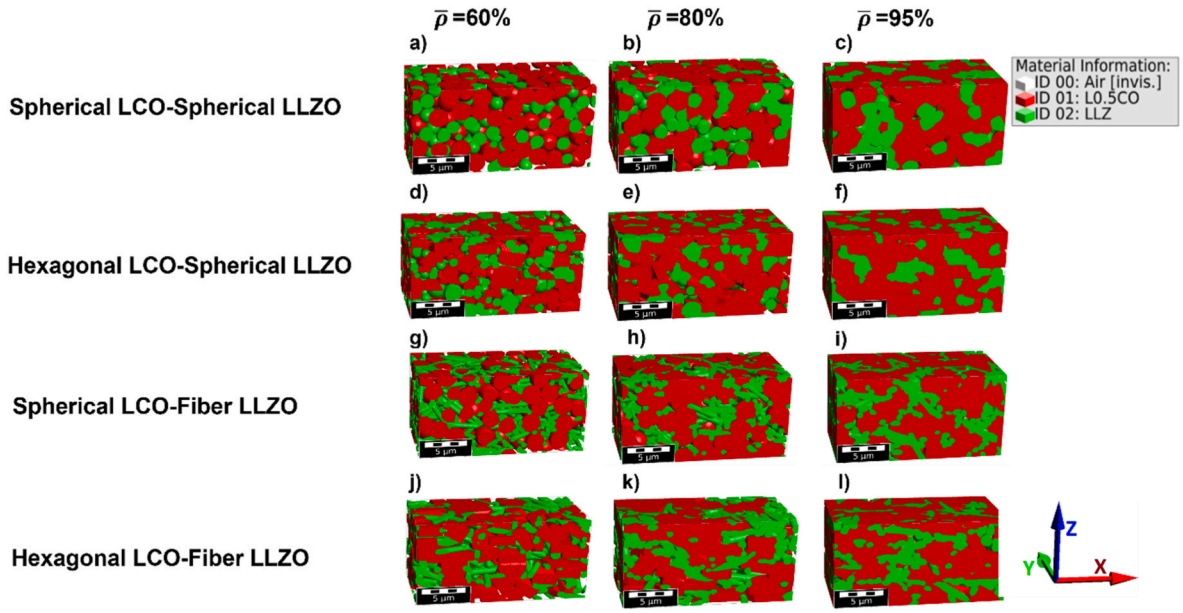


**Fig. 3.** Variation of $\bar{\rho}$ only (60, 80 and 95 %), a-c) spherical LCO-spherical LLZO. d-f) hexagonal LCO-spherical LLZO. g-i) spherical LCO-fiber LZO. j-l) hexagonal LCO-fiber LLZO. The fixed parameter values were as follow: $SVF_{LCO}$ = 69.4 %, average grain size of LCO and LLZO 2.00 μm and 1.43 μm, respectively, fiber LLZO length and diameters 3 μm and 0.5 μm, respectively.

$SVF_{LCO}$ (Fig. 4.).

The orientation of spherical LCO grains cannot be precisely controlled. Fig. 5b shows the orientation of spherical LCO grains from the x-axis, closely reflecting real-life conditions, while Fig. 5a depicts a similar structure with aligned orientations of spherical LCO grains. It is worth noting that the LLZO grains are aligned at 0° with respect to the x-axis, due to their isotropic structure. We investigated the mechanical stress induced in both configurations. In the case of aligned LCO spheres, the LCO grains can expand freely as the solid volume fraction increases, which lowers the induced compressive mechanical stress in LCO, while the remaining LLZO grains experience higher tensile stress (Fig. 5c). However, in randomly oriented spherical LCO grains, the axes of neighboring LCO grains may conflict (e.g., the c-axis of one LCO grain may oppose the a- or b-axis of another LCO grain), restricting LCO's ability to expand. As a result, LCO grains will suffer from an induced compressive mechanical stress (Fig. 5d). The induced compressive mechanical stress in LCO grains continues to increases with rising solid volume fraction of LCO since the LCO grains which substitute the LLZO ones have similar shrinking behavior of LLZO (Fig. 4). Furthermore, the compressive mechanical stress induced in LCO due to random LCO grain orientations is higher than that induced by LLZO, which is attributed to the larger strain values along the a- and b-axes of LCO compared to LLZO.

On the other hand, the behavior of the induced mechanical stress in LLZO follows the trend influenced by the increasing solid volume fraction of LCO. As spherical LLZO grains are gradually replaced by randomly oriented spherical LCO grains, the remaining LLZO grains exhibit an induced tensile mechanical stress, which intensifies as the LCO volume fraction increases (Fig. 4). When aligned spherical LCO is used, LLZO grains are surrounded by LCO grains. Parts of LLZO grains are in contact with the c-axis of neighboring LCO, which is expanding, thereby inducing tensile mechanical stress in the LLZO. Meanwhile, other parts of the LLZO grains contact to a surface parallel to a- or b-axis of LCO, which are under contraction, inducing compressive mechanical stress that counteracts the tensile stress (Fig. 5c). In contrast, when randomly oriented spherical LCO is present, the LLZO grains are in contact the expanding surface parallel to c-axis of LCO, leading to amplified tensile stress in LLZO (Fig. 5d).

When LCO grains with textured hexagonal planar structures are used, most LCO grains exhibit similar orientations where {001} facets are perpendicular to the c-axis. This sufficiently reduce the effect of random grain orientations on the induced mechanical stress. As a result,

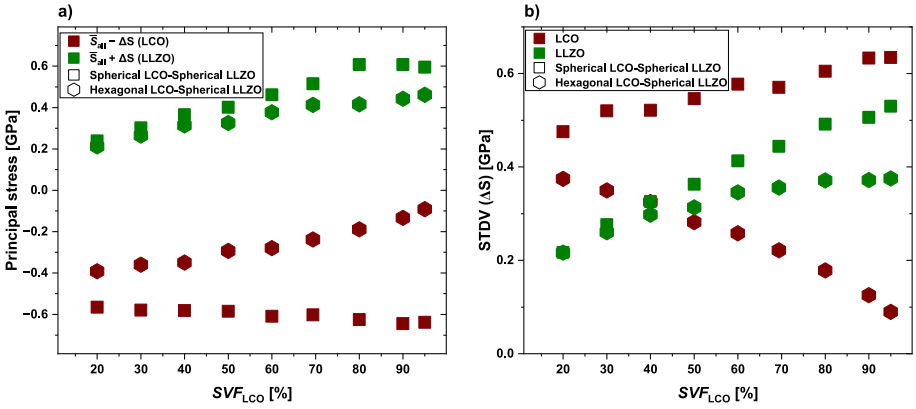


**Fig. 4.** a) Chemo-thermal principal stress as a function of the solid volume fraction of LCO ($SVF_{LCO}$) for random oriented spherical LCO-spherical LLZO and textured hexagonal LCO-spherical LLZO. b) The standard deviation, which represents the width of the distribution.

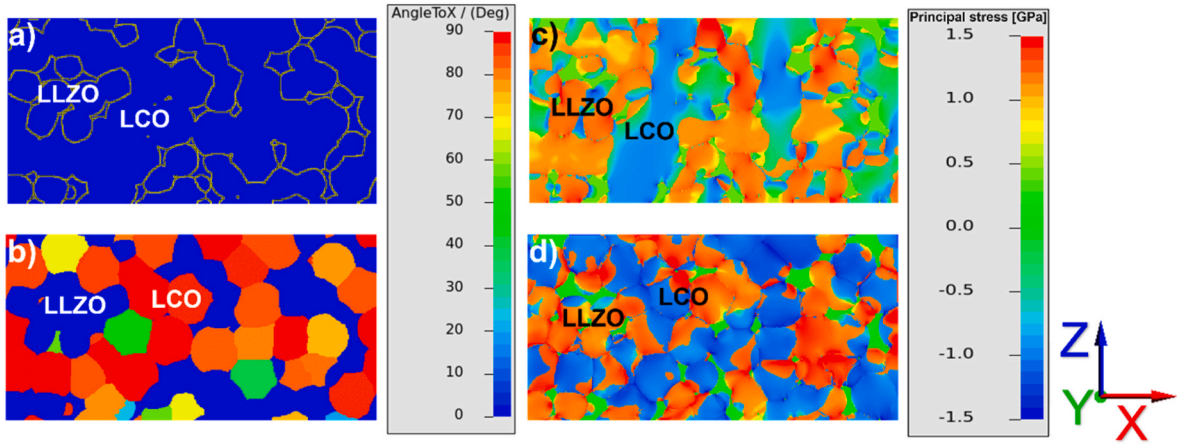


**Fig. 5.** a and b) Distribution of the angle to x-axis of LCO and LLZO grains for aligned spherical LCO-spherical LLZO and random oriented spherical LCO-spherical LLZO respectively. c and d) distribution of principal stress of tailored spherical LCO-spherical LLZO and random oriented spherical LCO-spherical LLZO respectively.

LCO can undergo volume changes freely, without constraints from neighboring grains, as the solid volume fraction of LCO increases. Consequently, the expected reduction in the induced compressive mechanical stress in LCO grains is observed (Fig. 4). However, the remaining LLZO grains experience higher induced tensile mechanical stress as the LCO volume fraction increases (Fig. 4).

Compared to the random oriented spherical LCO-spherical LLZO structure, the textured hexagonal LCO-spherical LLZO system exhibits lower induced mechanical stress, which is attributed to the absence of the impact of the random orientation of spherical LCO grains. It is worth mentioning that the key distinction between spherical and hexagonal LCO grains lies not in their shape but in the ability of flat hexagonal particles to be aligned during fabrication. If both grain types could be texturally aligned, they would exhibit similar mechanical results.

### 3.1.2. *Effect of fiber LLZO*

In this section, we investigated the influence of incorporating fiber LLZO on the induced mechanical stress in the system, considering variations in the LCO grain shape between random oriented spherical and textured hexagonal forms.

As the solid volume fraction of LCO increases in both the hexagonal LCO-spherical LLZO and hexagonal LCO-fiber LLZO systems, the mechanical stresses induced in LCO decreases while those in LLZO increase. Nevertheless, the hexagonal-fiber system exhibits reduced induced mechanical stresses for both LCO and LLZO compared to the hexagonal-spherical system (Fig. 6).

LCO exhibits anisotropic lattice change and is in textured alignment. Hence, an effect of the alignment of fiber LLZO on the mechanical stresses can be expected. Therefore, we generated a series of hexagonal-LCO-fiber LLZO microstructures, maintaining the hexagonal LCO grains in a textured orientation while systematically varying the alignment of the LLZO fibers at 0°, 45°, and 90° relative to the x-axis Fig. 7a and b and c respectively.

For each set, we analyzed the effect of increasing the solid volume fraction of LCO on the induced mechanical stresses in both LCO and LLZO. When the fiber LLZO was aligned horizontally, parallel to the x-axis, LCO exhibited higher induced tensile mechanical stress, while LLZO experienced higher induced compressive mechanical stress compared to the system which utilizes fiber LLZO with random orientation (Fig. 8a–e), indicating a stress inversion compared to the system with randomly aligned fibers. In this case, the fiber LLZO has greater contact with the {001} facets of hexagonal LCO, where the a- and b-axes undergo significant contractions with higher strain compared to LLZO. As a result, LLZO impedes the contraction of LCO, leading to induced tensile mechanical stress in LCO and compressive mechanical stress in LLZO. Conversely, fewer fiber's bases contact the {010} facets of hexagonal LCO grains, where the c-axis expands more actively, resulting in lower induced compressive mechanical stress in LCO and correspondingly lower tensile mechanical stress in LLZO.

A completely inverted behavior, with higher induced mechanical stresses, was observed when the fiber LLZO was aligned vertically, parallel to the z-axis. In this configuration, the LLZO fibers primarily contact the {010} facets of the hexagonal LCO grains, where the c-axis expansion is active, inducing compressive mechanical stress in LCO and

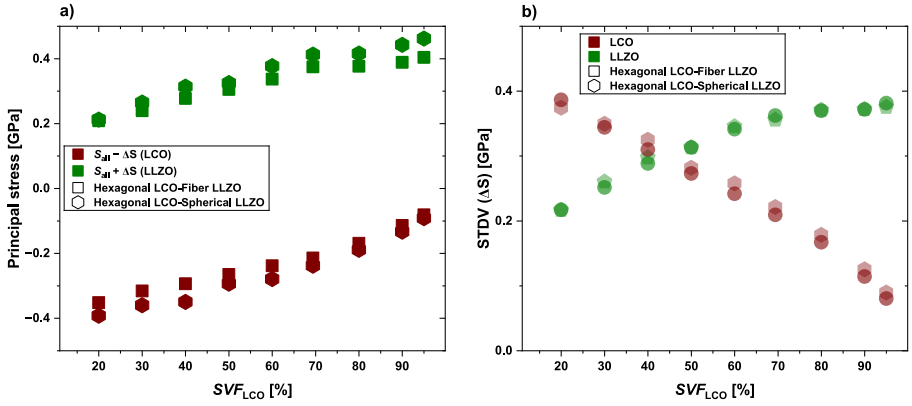


**Fig. 6.** a) Chemo-thermal principal stress as a function of the solid volume fraction of LCO ($SVF_{LCO}$) for textured hexagonal LCO-spherical LLZO and textured hexagonal LCO-fiber LLZO. b) The standard deviation, which represents the width of the distribution.

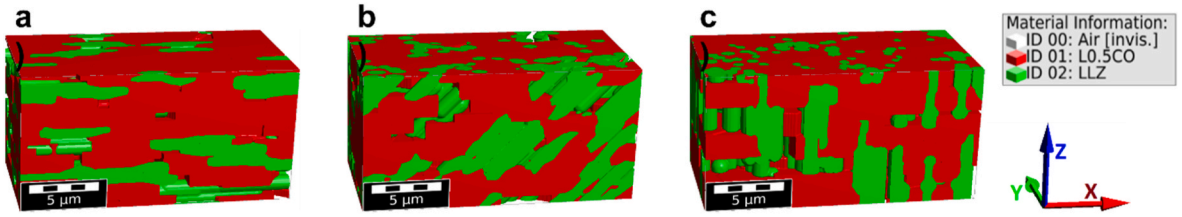


**Fig. 7.** Generated modeled microstructure utilizing textured hexagonal LCO and fiber LLZO while varying the alignment angles to the x-axis of fibers. a) 0°, b) 45°, c) 90°. $SVF_{LCO} = 69.4$ %, initial average grain size of LCO and LLZO 2.00 μm, the length and the diameter of fiber LLZO 3 μm and 0.5 μm respectively, and $\overline{\rho} = 93.14$ %.

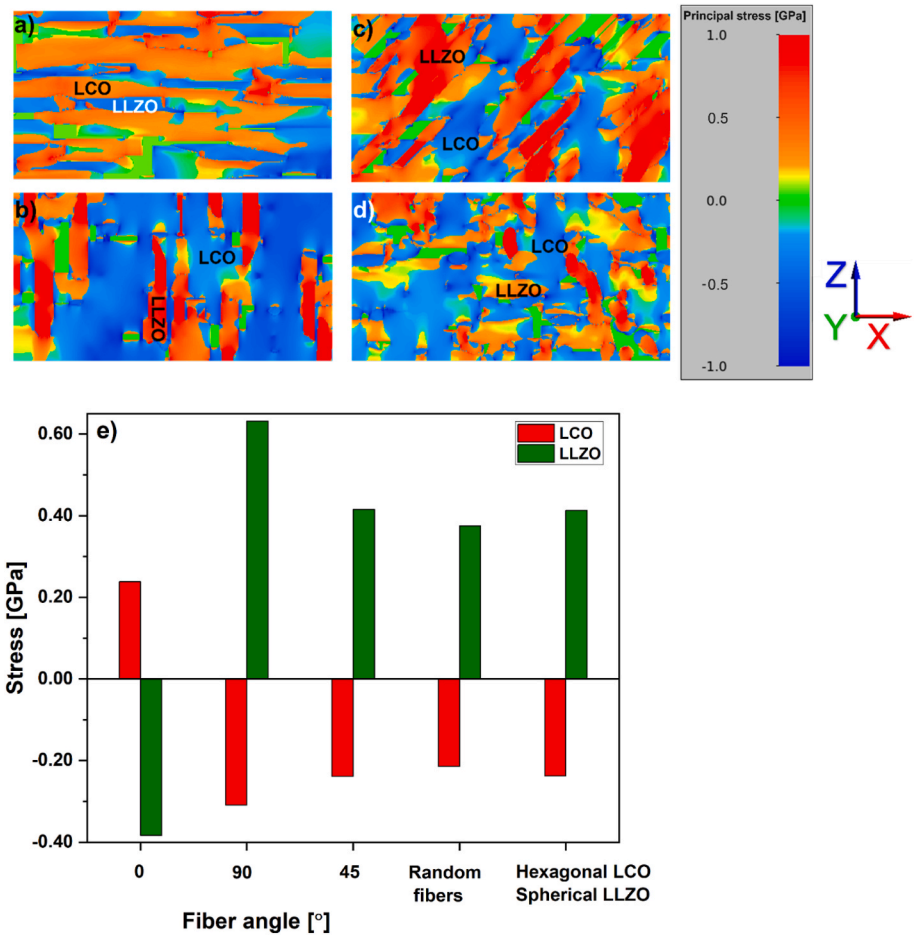


**Fig. 8.** Distribution of principal stress of textured hexagonal LCO-fiber LLZO while varying the alignment angles to the x-axis of fibers. a) 0°, b) 45°, c) 90° and d) randomly aligned. e) Bar chart illustrating the induced mechanical stress in LCO (red) and LLZO (green) as a function of fiber orientation (0°, 45°, 90° and random) and LLZO morphology (fibers vs. spherical). The results highlight the influence of fiber alignment and LLZO morphology on the induced mechanical stress within the composite cathode. $SVF_{LCO} = 69.4$ %, initial average grain size of LCO and LLZO 2.00 μm and 1.43 μm respectively, fiber LLZO length and diameters 3 μm and 0.5 μm respectively, and $\overline{\rho} = 93.14$ %. (For interpretation of the references to colour in this figure legend, the reader is referred to the Web version of this article.)

tensile mechanical stress in LLZO (Fig. 8b–e). Conversely, fewer LLZO fiber bases come into contact with the {001} facets of the hexagonal LCO grains, resulting in lower induced tensile mechanical stress in LCO and lower compressive mechanical stress in LLZO.

The system in which LLZO fibers are aligned 45° from x-axis, exhibits a similar behavior to the system in which the LLZO fibers are vertically aligned. However, in this case, more fiber bases are in contact with the {001} facets of the hexagonal LCO, leading to higher induced tensile mechanical stress in LCO and compressive mechanical stress in LLZO in both a and b-axes. This, in turn, contributes to a reduction in the higher induced compressive and tensile mechanical stresses in both LCO and LLZO, particularly along the c-axis attributed to increased contact between the fibers and the {010} facets of the hexagonal LCO grains, where c-axis expansion is active. Consequently, this leads to lower net induced compressive and tensile mechanical stresses in both LCO and LLZO, respectively (Fig. 8c–e).

In the previous three sets, although a similar number of hexagonal LCO and fiber LLZO grains were utilized, each configuration exhibited not only different behavior but also varying levels of induced mechanical stresses in both LCO and LLZO. Consequently, the facet-specific interface between LCO and LLZO grains is a key factor controlling the mechanical stresses observed in the system containing fiber LLZO. When LLZO fibers engage with the {001} facets of the hexagonal LCO grains, tensile mechanical stress in LCO and compressive mechanical stress in LLZO are induced. This configuration helps to reduce the induced compressive and tensile mechanical stresses of LCO and LLZO,

respectively.

While utilizing textured hexagonal LCO grains, fiber LLZO with random alignment exhibits lower induced mechanical stresses for both LCO and LLZO by 11.0 % and 9.0 % respectively, compared to the system utilizing spherical LLZO (Figs. 6 and 8e). This behavior can be attributed to the lower number of spherical grains that can come into contact with the {001} facets of hexagonal LCO. Consequently, this results in less reduction of the induced compressive and tensile mechanical stresses in both LCO and LLZO, which are mainly driven by the higher contact with the {010} facets of the hexagonal LCO grains. Furthermore, it is important to note that the results from the system where LLZO fibers are aligned at 45° from the x-axis are matching those of the spherical LLZO system (Fig. 8e), suggesting that these two systems exhibit equivalent mechanical behavior.

Despite the benefits of utilizing fiber LLZO, the orientation of LCO grains also plays a crucial role in limiting or even negating these advantages. This effect is more pronounced in systems using fiber LLZO combined with randomly oriented spherical LCO. In such cases, fiber LLZO predominantly contacts the regions of LCO where the c-axis is actively expanding, with fewer opportunities to engage with areas where the a- or b-axes are shrinking. As a result, the potential for reducing the induced mechanical stresses in the system is reduced, leading to higher induced tensile stress in LLZO as the solid volume fraction of LCO increases. On other hand, LCO grains exhibit higher induced mechanical stresses while increasing $SVF_{LCO}$ (Fig. 9). The induced compressive mechanical stresses in LCO exhibit a behavior similar to that of the previously discussed system utilizing spherical LCO and spherical LLZO. Therefore, a similar explanation for this behavior is applicable.

### 3.2. Grain morphology behavior with varying the relative density

The induced mechanical stress in both LCO and LLZO is exhibiting the convenient trend of varying the values of relative density [46]. In which the induced mechanical stress in LCO and LLZO are directly proportional to $\overline{\rho}$, ascribed to the higher coordination number (Figs. S2–S3).

In systems utilizing tailored hexagonal LCO, the induced mechanical stress in LCO is lower than that in LLZO (Figure S2 a,b), which can be attributed to the low volume fraction of LLZO in the system. On the other hand, systems which utilize random oriented spherical LCO exhibit higher induced stresses in both LCO and LLZO compared to those with tailored hexagonal LCO (Figs. S2 and S3), a result of the previously discussed effect of random orientation in LCO. Due to this effect, the sensitivity of mechanical stress in LCO to the variation of $\overline{\rho}$ is higher than the one in LLZO. Which in turn leads to higher induced mechanical stress in LCO than in LLZO (Figure S3 a,b) despite low volume fraction of LLZO in the system. Furthermore, while utilizing randomly oriented spherical LCO, the stress values in both LCO and LLZO are slightly higher for fiber LLZO compared to spherical LLZO, ascribed to the higher surface area of fiber LLZO.

## 4. Conclusions

In this study, we investigated the effect of the grain morphology in a composite cathode on the induced mechanical stress. Our finding shows that utilizing LLZO fiber with random alignments combined with textured hexagonal LCO reduced the induced mechanical stress in both LCO and LLZO by 11.0 % and 9.0 % respectively, compared to the systems utilizing spherical LLZO. The alignment of LLZO fibers significantly impacted the stress type in the system, due to the facet-specific contact interface between the LLZO and LCO grains. When fiber LLZO are in contact with the {001} facets of textured hexagonal LCO, tensile and compressive mechanical stresses in LCO and LLZO, respectively, are expected. On other hand, stresses are inverted when the LLZO fiber is in contact with the {010} facets of hexagonal LCO. Furthermore, we showed the preferable anisotropic expansion-contraction behavior in the CAM, which could be utilized to lower the induced mechanical stress in the system. This was more pronounced by utilizing fiber LLZO. However, the advantages which could gained by utilizing the impact of facet-specific contact interface between the solid electrolyte and the cathode active material grains are limited by the behavior of the cathode active material. Furthermore, it is not favorable to utilize spherical LCO, since its orientation cannot be guaranteed. The randomly oriented spherical LCO-spherical LLZO exhibits the highest induced mechanical stresses compared to the other investigated systems. Currently, all stress values presented in this study are obtained through theoretical calculations. A comprehensive experimental validation of the modeling methodology is underway using synchrotron measurements at the European Synchrotron Radiation Facility (ESRF) in Grenoble, France; however, the process remains highly challenging. Moreover, the experimental validation of the stiffness tensors, is not yet achievable. Accurate representation of microstructural features, including voxel size and interface resolution, plays a critical role in ensuring the reliability of property simulations. A detailed discussion of these aspects is provided in our previous work [46]. The impact of the morphology of the component's grains on the electronic and ionic conductivities of LCO and LLZO respectively will be the topic of investigation in the future work.

## CRediT authorship contribution statement

**Fadi Al-Jaljouli:** Writing – original draft, Visualization, Validation, Methodology, Investigation, Formal analysis, Data curation, Conceptualization. **Robert Mücke:** Writing – review & editing, Supervision,

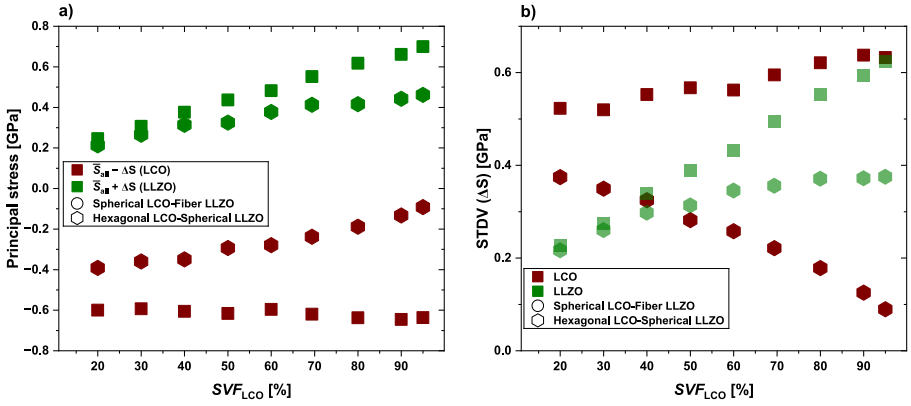


**Fig. 9.** Chemo-thermal principal stress as a function of the solid volume fraction of LCO ($SVF_{LCO}$) for textured hexagonal LCO-spherical LLZO and random oriented spherical LCO-fiber LLZO. b) The standard deviation, which represent the width of distribution.

Software, Methodology. **Martin Finsterbusch:** Writing – review & editing. **Payam Kaghazchi:** Writing – review & editing. **Olivier Guillon:** Writing – review & editing, Supervision, Project administration.

## Declaration of competing interest

The authors declare the following financial interests/personal relationships which may be considered as potential competing interests: Fadi Al-Jaljouli reports financial support was provided by Federal Ministry of Education and Research of Germany. Fadi Al-Jaljouli reports financial support was provided by Meet-HiEnD III. Payam Kaghazchi reports financial support was provided by Meet-HiEnD III. Martin Finsterbusch reports financial support was provided by Meet-HiEnD III. Martin Finsterbusch reports financial support was provided by FestBatt2-Oxide. If there are other authors, they declare that they have no known competing financial interests or personal relationships that could have appeared to influence the work reported in this paper.

## Acknowledgements

The financial support provided by the Federal Ministry of Education and Research of Germany in the framework of the Palestinian-German Science Bridge (PGSB) (BMBF Grant Number 01DH16027), FestBatt2-Oxide (grant no. 13XP0434A) and Meet-HiEnD III (grant no. 03XP0258Cs) is gratefully acknowledged.

## Appendix A. Supplementary data

Supplementary data to this article can be found online at https://doi.org/10.1016/j.jpowsour.2025.237539.

## Data availability

The data that has been used is confidential.

## References

[1] M. Finsterbusch, T. Danner, C.-L. Tsai, S. Uhlenbruck, A. Latz, O. Guillon, High capacity garnet-based all-solid-state lithium batteries: fabrication and 3D-Microstructure resolved modeling, ACS Appl. Mater. Interfaces 10 (26) (2018) 22329–22339, https://doi.org/10.1021/acsami.8b06705.

[2] R. Miyazaki, G. Yamaguchi, E. Yagi, T. Yoshida, T. Tomita, Enhancement of the li+ conductivity of $Li_3AlF_6$ for stable all-solid-state lithium-ion batteries, ACS Appl. Energy Mater. 7 (6) (2024) 2533–2541, https://doi.org/10.1021/acsaem.4c00115.

[3] K. Kerman, A. Luntz, V. Viswanathan, Y.-M. Chiang, Z. Chen, Review—practical challenges hindering the development of solid state li ion batteries, J. Electrochem. Soc. 164 (7) (2017) A1731, https://doi.org/10.1149/2.1571707jes.

[4] S. Wenzel, T. Leichtweiss, D. Krüger, J. Sann, J. Janek, Interphase formation on lithium solid electrolytes—An in situ approach to study interfacial reactions by photoelectron spectroscopy, Solid State Ionics 278 (2015) 98–105, https://doi.org/10.1016/j.ssi.2015.06.001.

[5] P. Bron, B. Roling, S. Dehnen, Impedance characterization reveals mixed conducting interphases between sulfidic superionic conductors and lithium metal electrodes, J. Power Sources 352 (2017) 127–134, https://doi.org/10.1016/j.jpowsour.2017.03.103.

[6] S. Wenzel, S. Randau, T. Leichtweiß, D.A. Weber, J. Sann, W.G. Zeier, J.r. Janek, Direct observation of the interfacial instability of the fast ionic conductor $Li_{10}GeP_2S_{12}$ at the lithium metal anode, Chem. Mater. 28 (7) (2016) 2400–2407, https://doi.org/10.1021/acs.chemmater.6b00610.

[7] T. Yang, J. Zheng, Q. Cheng, Y.Y. Hu, C.K. Chan, Composite polymer electrolytes with $Li_7La_3Zr_2O_{12}$ garnet-type nanowires as ceramic fillers: mechanism of conductivity enhancement and role of doping and morphology, ACS Appl. Mater. Interfaces 9 (26) (2017) 21773–21780, https://doi.org/10.1021/acsami.7b03806.

[8] F. Aguesse, W. Manalastas, L. Buannic, J.M. Lopez del Amo, G. Singh, A. Llordés, J. Kilner, Investigating the dendritic growth during full cell cycling of garnet electrolyte in direct contact with Li metal, ACS Appl. Mater. Interfaces 9 (4) (2017) 3808–3816, https://doi.org/10.1021/acsami.6b13925.

[9] R.H. Basappa, T. Ito, T. Morimura, R. Bekarevich, K. Mitsuishi, H. Yamada, Grain boundary modification to suppress lithium penetration through garnet-type solid electrolyte, J. Power Sources 363 (2017) 145–152, https://doi.org/10.1016/j.jpowsour.2017.07.088.

[10] A. Sharafi, H.M. Meyer, J. Nanda, J. Wolfenstine, J. Sakamoto, Characterizing the Li–$Li_7La_3Zr_2O_{12}$ interface stability and kinetics as a function of temperature and current density, J. Power Sources 302 (2016) 135–139, https://doi.org/10.1016/j.jpowsour.2015.10.053.

[11] A. Bates, S. Mukherjee, N. Schuppert, B. Son, J.G. Kim, S. Park, Modeling and simulation of 2D lithium-ion solid state battery, Int. J. Energy Res. 39 (11) (2015) 1505–1518, https://doi.org/10.1002/er.3344.

[12] G. Bucci, T. Swamy, S. Bishop, B.W. Sheldon, Y.-M. Chiang, W.C. Carter, The effect of stress on battery-electrode capacity, J. Electrochem. Soc. 164 (4) (2017) A645, https://doi.org/10.1149/2.0371704jes.

[13] G. Bucci, T. Swamy, Y.-M. Chiang, W.C. Carter, Modeling of internal mechanical failure of all-solid-state batteries during electrochemical cycling, and implications for battery design, J. Mater. Chem. A 5 (36) (2017) 19422–19430, https://doi.org/10.1039/C7TA03199H.

[14] A. Mukhopadhyay, B.W. Sheldon, Deformation and stress in electrode materials for Li-ion batteries, Prog. Mater. Sci. 63 (2014) 58–116, https://doi.org/10.1016/j.pmatsci.2014.02.001.

[15] Y. He, C. Lu, S. Liu, W. Zheng, J. Luo, Interfacial incompatibility and internal stresses in all-solid-state lithium ion batteries, Adv. Energy Mater. 9 (36) (2019) 1901810, https://doi.org/10.1002/aenm.201901810.

[16] P. Li, Y.B. Zhao, Y.X. Shen, S.H. Bo, Fracture behavior in battery materials, JPhys Energy 2 (2) (2020), https://doi.org/10.1088/2515-7655/ab83e1.

[17] K. Mukai, Zero-strain insertion materials for all-solid-state Li-Ion batteries, in: R. Murugan, W. Weppner (Eds.), Solid Electrolytes for Advanced Applications: Garnets and Competitors, Springer International Publishing, Cham, 2019, pp. 219–240.

[18] F. Strauss, L. de Biasi, A.Y. Kim, J. Hertle, S. Schweidler, J. Janek, P. Hartmann, T. Brezesinski, Rational design of quasi-zero-strain NCM cathode materials for minimizing volume change effects in all-solid-state batteries, ACS Mater. Lett. 2 (1) (2020) 84–88, https://doi.org/10.1021/acsmaterialslett.9b00441.

[19] K. Mukai, Pseudo zero-strain insertion materials for Li-ion batteries: cross-sectional observations of $LiNi_{1/2}Co_{1/2}O_2$, $LiNi_{1/3}Co_{1/3}Mn_{1/3}O_2$, and $LiNi_{0.8}Co_{0.15}Al_{0.05}O_2$, Ionics 24 (8) (2018) 2181–2186, https://doi.org/10.1007/s11581-017-2385-2.

[20] R. Koerver, W. Zhang, L. de Biasi, S. Schweidler, A.O. Kondrakov, S. Kolling, T. Brezesinski, P. Hartmann, W.G. Zeier, J. Janek, Chemo-mechanical expansion of lithium electrode Materials–On the route to mechanically optimized all-solid-state batteries, Energy Environ. Sci. 11 (8) (2018) 2142–2158, https://doi.org/10.1039/C8EE00907D.

[21] G. Liu, H. Zheng, S. Kim, Y. Deng, A. Minor, X. Song, V.S. Battaglia, Effects of various conductive additive and polymeric binder contents on the performance of a lithium-ion composite cathode, J. Electrochem. Soc. 155 (12) (2008) A887, https://doi.org/10.1149/1.2976031.

[22] B. Ludwig, Z. Zheng, W. Shou, Y. Wang, H. Pan, Solvent-free manufacturing of electrodes for lithium-ion batteries, Sci. Rep. 6 (1) (2016) 1–10, https://doi.org/10.1038/srep23150.

[23] Y. He, P. Xu, D. Jiang, H. Hu, D. Li, S. Shi, Quantifying the solid electrolyte interphase stress induced capacity fading of lithium-ion batteries via a multiscale mechanical-electrochemical coupling model, Sci. China Technol. Sci. 67 (10) (2024) 3168–3181, https://doi.org/10.1007/s11431-024-2711-7.

[24] J. Auborn, Y. Barberio, Lithium intercalation cells without metallic lithium: $MoO_2$ and $WO_2$/$LiCoO_2$, J. Electrochem. Soc. 134 (3) (1987) 638, https://doi.org/10.1149/1.2100521.

[25] T. Nagaura, K. Tozawa, Progress in Batteries and Solar Cells, vol. 9, JEC Press, 1990, p. 209, https://doi.org/10.1541/ieejfms1990.115.4_349.

[26] B. Wang, J. Bates, F. Hart, B. Sales, R. Zuhr, J. Robertson, Characterization of thin-film rechargeable lithium batteries with lithium cobalt oxide cathodes, J. Electrochem. Soc. 143 (10) (1996) 3203, https://doi.org/10.1149/1.1837188.

[27] A. Kannan, L. Rabenberg, A. Manthiram, High capacity surface-modified $LiCoO_2$ cathodes for lithium-ion batteries, Electrochem. Solid State Lett. 6 (1) (2002) A16, https://doi.org/10.1149/1.1526782.

[28] Y.J. Kim, H. Kim, B. Kim, D. Ahn, J.-G. Lee, T.-J. Kim, D. Son, J. Cho, Y.-W. Kim, B. Park, Electrochemical stability of thin-film $LiCoO_2$ cathodes by aluminum-oxide coating, Chem. Mater. 15 (7) (2003) 1505–1511, https://doi.org/10.1021/cm0201403.

[29] C. Daniel, D. Mohanty, J. Li, D.L. Wood, Cathode materials review, AIP Conf. Proc. 1597 (1) (2014) 26–43, https://doi.org/10.1063/1.4878478.

[30] C. Wang, G. Bai, X. Liu, Y. Li, Favorable electrochemical performance of $LiMn_2O_4$/$LiFePO_4$ composite electrodes attributed to composite solid electrolytes for all-solid-state lithium batteries, Langmuir 37 (7) (2021) 2349–2354, https://doi.org/10.1021/acs.langmuir.0c03274.

[31] R. Murugan, V. Thangadurai, W. Weppner, Fast lithium ion conduction in garnet-type $Li_7La_3Zr_2O_{12}$, ANGEW. CHEM. INT. EDITION IN ENGLISH 46 (41) (2007) 7778, https://doi.org/10.1002/anie.200701144.

[32] C.-L. Tsai, E. Dashjav, E.-M. Hammer, M. Finsterbusch, F. Tietz, S. Uhlenbruck, H. P. Buchkremer, High conductivity of mixed phase Al-substituted $Li_7La_3Zr_2O_{12}$, J. Electroceram. 35 (1) (2015) 25–32, https://doi.org/10.1007/s10832-015-9988-7.

[33] H. Buschmann, J. Dölle, S. Berendts, A. Kuhn, P. Bottke, M. Wilkening, P. Heitjans, A. Senyshyn, H. Ehrenberg, A. Lotnyk, Structure and dynamics of the fast lithium ion conductor "$Li_7La_3Zr_2O_{12}$", Phys. Chem. Chem. Phys. 13 (43) (2011) 19378–19392, https://doi.org/10.1039/C1CP22108F.

[34] C.-L. Tsai, V. Roddatis, C.V. Chandran, Q. Ma, S. Uhlenbruck, M. Bram, P. Heitjans, O. Guillon, $Li_7La_3Zr_2O_{12}$ interface modification for Li dendrite prevention, ACS Appl. Mater. Interfaces 8 (16) (2016) 10617–10626, https://doi.org/10.1021/acsami.6b00831.

[35] F. Yonemoto, A. Nishimura, M. Motoyama, N. Tsuchimine, S. Kobayashi, Y. Iriyama, Temperature effects on cycling stability of Li plating/stripping on Ta-doped $Li_7La_3Zr_2O_{12}$, J. Power Sources 343 (2017) 207–215, https://doi.org/10.1016/j.jpowsour.2017.01.009.

[36] L. Miara, A. Windmüller, C.-L. Tsai, W.D. Richards, Q. Ma, S. Uhlenbruck, O. Guillon, G. Ceder, About the compatibility between high voltage spinel cathode materials and solid oxide electrolytes as a function of temperature, ACS Appl. Mater. Interfaces 8 (40) (2016) 26842–26850, https://doi.org/10.1021/acsami.6b09059.

[37] K.H. Kim, Y. Iriyama, K. Yamamoto, S. Kumazaki, T. Asaka, K. Tanabe, C.A. J. Fisher, T. Hirayama, R. Murugan, Z. Ogumi, Characterization of the interface between $LiCoO_2$ and $Li_7La_3Zr_2O_{12}$ in an all-solid-state rechargeable lithium battery, J. Power Sources 196 (2) (2011) 764–767, https://doi.org/10.1016/j.jpowsour.2010.07.073.

[38] W.D. Richards, L.J. Miara, Y. Wang, J.C. Kim, G. Ceder, Interface stability in solid-state batteries, Chem. Mater. 28 (2016) 266–273, https://doi.org/10.1021/acs.chemmater.5b04082.

[39] H. Jeon, D.-H. Kwon, H. Kim, J.-H. Lee, Y. Jun, J.-W. Son, S. Park, Tailoring shape and exposed crystal facet of single-crystal layered-oxide cathode particles for all-solid-state batteries, Chem. Eng. J. 445 (2022) 136828, https://doi.org/10.1016/j.cej.2022.136828.

[40] N. Wu, Y. Zhang, Y. Guo, S. Liu, H. Liu, H. Wu, Flakelike $LiCoO_2$ with Exposed {010} Facets As a Stable Cathode Material for Highly Reversible Lithium Storage, ACS Appl. Mater. Interfaces 8 (4) (2016) 2723–2731, https://doi.org/10.1021/acsami.5b10977.

[41] M.J. Counihan, D.J. Powers, P. Barai, S. Hu, T. Zagorac, Y. Zhou, J. Lee, J. G. Connell, K.S. Chavan, I.S. Gilmore, L. Hanley, V. Srinivasan, Y. Zhang, S. Tepavcevic, Understanding the influence of $Li_7La_3Zr_2O_{12}$ nanofibers on critical current density and coulombic efficiency in composite polymer electrolytes, ACS Appl. Mater. Interfaces 15 (21) (2023) 26047–26059, https://doi.org/10.1021/acsami.3c04262.

[42] Z. Wan, D. Lei, W. Yang, C. Liu, K. Shi, X. Hao, L. Shen, W. Lv, B. Li, Q.-H. Yang, F. Kang, Y.-B. He, Low resistance–integrated all-solid-state battery achieved by $Li_7La_3Zr_2O_{12}$ nanowire upgrading polyethylene oxide (PEO) composite electrolyte and PEO cathode binder, Adv. Funct. Mater. 29 (1) (2019) 1805301, https://doi.org/10.1002/adfm.201805301.

[43] D.O. Shin, K. Oh, K.M. Kim, K.-Y. Park, B. Lee, Y.-G. Lee, K. Kang, Synergistic multi-doping effects on the $Li_7La_3Zr_2O_{12}$ solid electrolyte for fast lithium ion conduction, Sci. Rep.Uk 5 (1) (2015) 18053, https://doi.org/10.1038/srep18053.

[44] L. Zhong, J. Li, Z.-x. Chen, L.-p. Zhou, H.-x. Liu, X.-q. Shen, M.-x. Jing, A LLZO Fibers/PPO polymeric matrix solid electrolyte for high voltage solid-state lithium batteries, Appl. Phys. A 130 (9) (2024) 662, https://doi.org/10.1007/s00339-024-07815-x.

[45] W. He, H. Ding, X. Chen, W. Yang, Three-dimensional LLZO/PVDF-HFP fiber network-enhanced ultrathin composite solid electrolyte membrane for dendrite-free solid-state lithium metal batteries, J. Membr. Sci. 665 (2023) 121095, https://doi.org/10.1016/j.memsci.2022.121095.

[46] F. Al-Jaljouli, R. Mücke, P. Kaghazchi, Y.J. Sohn, M. Finsterbusch, D. Fattakhova-Rohlfing, O. Guillon, Microstructural parameters governing the mechanical stress and conductivity of all-solid-state lithium-ion-battery cathodes, J. Energy Storage 68 (2023) 107784, https://doi.org/10.1016/j.est.2023.107784.

[47] M. Mann, M. Küpers, G. Häuschen, M. Finsterbusch, D. Fattakhova-Rohlfing, O. Guillon, The influence of hafnium impurities on the electrochemical performance of tantalum substituted $Li_7La_3Zr_2O_{12}$ solid electrolytes, Ionics 28 (1) (2022) 53–62, https://doi.org/10.1007/s11581-021-04300-w.

[48] M. Mann, M. Küpers, G. Häuschen, M. Finsterbusch, D. Fattakhova-Rohlfing, O. Guillon, Evaluation of scalable synthesis methods for aluminum-substituted $Li_7La_3Zr_2O_{12}$ solid electrolytes, Materials 14 (22) (2021) 6809, https://doi.org/10.3390/ma14226809.

[49] R. Mücke, M. Finsterbusch, P. Kaghazchi, D. Fattakhova-Rohlfing, O. Guillon, Modelling electro-chemical induced stresses in all-solid-state batteries: anisotropy effects in cathodes and cell design optimisation, J. Power Sources 489 (2021) 229430, https://doi.org/10.1016/j.jpowsour.2020.229430.

[50] M. Tanemura, T. Ogawa, N. Ogita, A new algorithm for three-dimensional voronoi tessellation, J. Comput. Phys. 51 (2) (1983) 191–207, https://doi.org/10.1016/0021-9991(83)90087-6.

[51] E.J. Cheng, N.J. Taylor, J. Wolfenstine, J. Sakamoto, Elastic properties of lithium cobalt oxide ($LiCoO_2$), J. Asian Ceram. Soc. 5 (2) (2017) 113–117, https://doi.org/10.1016/j.jascer.2017.03.001.

[52] S. Yamakawa, N. Nagasako, H. Yamasaki, T. Koyama, R. Asahi, Phase-field modeling of stress generation in polycrystalline $LiCoO_2$, Solid State Ionics 319 (2018) 209–217, https://doi.org/10.1016/j.ssi.2018.02.013.

[53] A.-N. Wang, J.F. Nonemacher, G. Yan, M. Finsterbusch, J. Malzbender, M. Krüger, Mechanical properties of the solid electrolyte Al-substituted $Li_7La_3Zr_2O_{12}$ (LLZO) by utilizing micro-pillar indentation splitting test, J. Eur. Ceram. Soc. 38 (9) (2018) 3201–3209, https://doi.org/10.1016/j.jeurceramsoc.2018.02.032.

[54] J.E. Ni, E.D. Case, J.S. Sakamoto, E. Rangasamy, J.B. Wolfenstine, Room temperature elastic moduli and vickers hardness of hot-pressed LLZO cubic garnet, J. Mater. Sci. 47 (23) (2012) 7978–7985, https://doi.org/10.1007/s10853-012-6687-5.

[55] S. Yu, R.D. Schmidt, R. Garcia-Mendez, E. Herbert, N.J. Dudney, J.B. Wolfenstine, J. Sakamoto, D.J. Siegel, Elastic properties of the solid electrolyte $Li_7La_3Zr_2O_{12}$ (LLZO), Chem. Mater. 28 (1) (2016) 197–206, https://doi.org/10.1021/acs.chemmater.5b03854.

[56] H. Moulinec, P. Suquet, A numerical method for computing the overall response of nonlinear composites with complex microstructure, Comput. Methods Appl. Mech. Eng. 157 (1) (1998) 69–94, https://doi.org/10.1016/S0045-7825(97)00218-1.

[57] M. Schneider, F. Ospald, M. Kabel, Computational homogenization of elasticity on a staggered grid, Int. J. Numer. Methods Eng. 105 (9) (2016) 693–720, https://doi.org/10.1002/nme.5008.